

Effect of Winglet Cant Angle on Lift-to-Drag Ratio

Borg, Auston J. Lam, Brandon H. Latzko, Alexander J.

Section 11832 December 6, 2023

Abstract—This study examines the relationship between the cant angle of a winglet and the lift-to-drag ratio of the airfoil section by using a calibrated dynamometer. The main objective of this experiment was to create a model for the relationship between the cant angle and the lift-to-drag ratio, L/D . A secondary objective was to determine if adjusting the cant angle could lead to an optimal angle for maximizing the lift-to-drag ratio of the airfoil section. Winglets disrupt the formation of wingtip vortices and force the airflow to become more two-dimensional, reducing the induced drag of the wing. Unlike other wing features such as flaps and ailerons, winglets cannot be adjusted during flight to provide the most optimal setting for the aircraft. The theory behind this experiment is that by adjusting the cant angle, the most optimal performance during simulated cruise conditions can be achieved. It was found that the optimal cant angle for the performance of the wing was $42 \pm 1^\circ$. The relative difference between theoretical data obtained using XFLR5 and the experimental data ranged from 6.4% to 14.1% for the values of the lift-to-drag ratio. This was caused by the surface roughness of the 3D printed wing section and the mounting equipment used to attach it to the dynamometer. The results showed that the lift-to-drag ratio slightly increased with the cant angle until reaching its optimal value, after which the parasitic drag caused by the attachment causes the ratio to decline in magnitude.

Index Terms—cant angle, lift-to-drag ratio, winglet, XFLR5

I. INTRODUCTION

In the field of commercial aviation, more than 45,000 planes take off each day [1]. To reduce costs and promote more sustainable flights, airlines have consistently sought out ways to enhance the efficiency of their aircraft. One important measure of an aircraft's efficiency is its lift-to-drag ratio. A high lift-to-drag ratio allows an aircraft to carry larger payloads while requiring less thrust to overcome drag. One technique used in modern aircraft is the addition of winglets to the tips of the wings. These winglets disrupt the wingtip vortices and force the airflow to become more two-dimensional, reducing the induced drag on the wing [2]. Despite their use in the aviation industry for many years, there is a surprising lack of publications providing specific details on efficient winglet design. One consideration in winglet design is the winglet cant angle, which is the angle that the winglet makes with the span of the wing, as shown in Fig. 1.

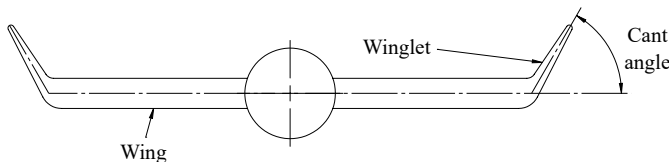


Fig. 1. A simplified diagram that illustrates how the cant angle relates the orientation of the winglet to the span of the wing [3].

Previous research has suggested that the lift-to-drag ratio generally increases with the cant angle. However, once the cant angle passes a certain point, the increase in friction drag begins to decrease the aerodynamic efficiency [4].

The experiment involved creating 3D printed wings with interchangeable winglets. These winglets had varying cant angles, ranging from 0 to 90 degrees. Fig. 2 shows an example of one of these wings.



Fig. 2. A 3D printed model of the wing used in the experiment. The specific configuration shown has a cant angle of 40° .

The wind tunnel was adjusted to a desired Reynolds number of 100,000 by using the tunnel calibration coefficient determined previously [5]. The desired drop in static pressure was related to the Reynolds number using (1), where K is the tunnel calibration coefficient, ν is the dynamic viscosity of air, ρ is the density of the air, c is the chord length of the airfoil, and Re is the desired Reynolds number.

$$\Delta P = \frac{\frac{1}{2} \rho (1 - K) \nu^2}{c^2} Re^2 \quad (1)$$

The objectives of this experiment included first characterizing the relationship between the winglet cant angle and the lift-to-drag ratio of a wing by determining an equation that properly represents the experimental data. The second objective was to use this equation to determine the optimal cant angle that maximizes the lift-to-drag ratio. Finally, the software XFLR5 was also used to compare theoretical data to experimental data.

II. PROCEDURE

A. Manufacturing of the Wing

The wing was 3D printed using a fused deposition modeling (FDM) printer in ASA thermoplastic. The model for the 3D print was created using the CAD software SolidWorks. It was divided into three sections, consisting of the wing base and two winglets. The selected airfoil was the NACA2415, and the

wing was set at an angle of attack of 10 degrees. This angle of attack was selected to ensure that a non-negligible lift force would be generated by the airfoil. The wing base was designed with two hexagonal pins on each side, which were intended to press fit into the corresponding holes on the winglet pieces, as depicted in Fig. 3.

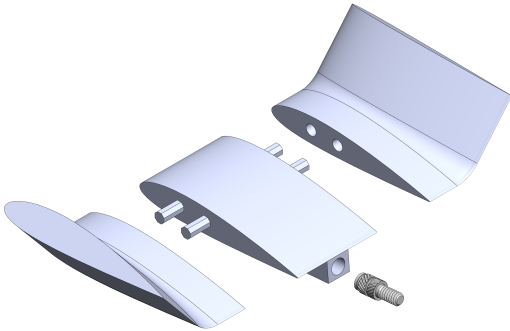


Fig. 3. SolidWorks 3D model of the wing section used in this experiment. The specific configuration shown has a cant angle of 50°.

The winglet pieces had ten different configurations with cant angles ranging from 0 to 90 degrees. Each configuration maintained a constant wingspan to ensure consistency across trials. A total of twenty winglet pieces were manufactured, with ten for each side of the wing. The chord length of the airfoil was 76.2 ± 0.2 mm, and the wingspan of the airfoil section was 139.8 ± 0.2 mm, as measured with calipers. A 10-24 male heat-set insert was mounted onto the wing base to allow for proper threading of the wing into the 10-24 threaded hole in the dynamometer.

B. Calibration of the Dynamometer

For this experiment, the dynamometer was calibrated for both lift and drag. To perform the calibration, metal weights were weighed using a scale. Once the weights were recorded, they were placed on the dynamometer, which was set up in a configuration such that the weight would be loaded perpendicular to the length of the stand for drag calculation, as shown in Fig. 4.



Fig. 4. Dynamometer setup for calibrating the drag calculation with a 500 g weight loaded.

A total of twelve different mass configurations were measured, ranging from 0.000 kg to 2.270 kg. The maximum mass corresponds to the maximum force that the dynamometer can measure. The weights were attached to the dynamometer using a hook attached to the weight itself. Additional weights needed to reach the desired weight were attached to the bottom of each weight using the hook.

To zero the drag force, the drag LVDT wheel was adjusted until the voltage display read zero when no weight was loaded. Then, the maximum weight was placed on the dynamometer and the gain potentiometer was adjusted until a voltage of -10 V was displayed. The weights were then removed, and the display was verified to show zero voltage. This process was repeated for each weight configuration.

The same procedure was performed for the lift calibration, except this time the desired maximum voltage for the zero verification was 10 V. The dynamometer was also reoriented so that the weights acted parallel to the length of the dynamometer, in the lift direction by threading an eyebolt, as shown in Fig. 5. The slope of the line obtained from both calibrations was then used to determine force values for the experiment.

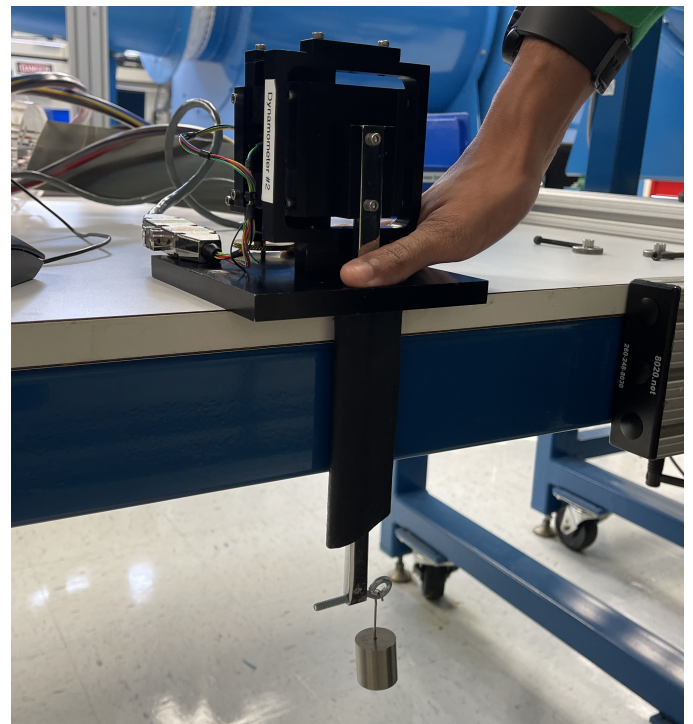


Fig. 5. Dynamometer setup for calibrating the lift calculation with a 200 g weight loaded.

C. Measuring Lift and Drag

The ambient pressure, relative humidity, and ambient temperature were recorded. To measure the air velocity in the wind tunnel, the pressure transducer was calibrated in inches of water in the negative direction using the digital readout on the transducer and a water manometer. The desired Reynolds number for this experiment was 100,000 to simulate cruise conditions for an RC aircraft with the same chord length. To achieve this, the wind tunnel speed was adjusted until the

pressure readout matched the desired static gauge pressure for the current ambient conditions. The zero drag and lift weight of the dynamometer were then recorded by placing the dynamometer in the wind tunnel and recording the voltages displayed on the pressure transducer. The wing base section was positioned in the test section by using the 10-24 male heat-set insert located at the back of the central span. Next, the appropriate winglet pieces with the specific cant angle were attached to the wing base, as shown in Fig. 6.

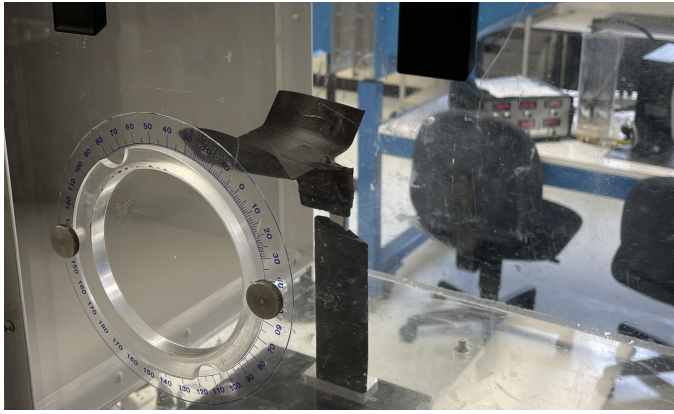


Fig. 6. Wing section with the 40° winglets inside the test section of the wind tunnel.

The wind tunnel was set to the previously determined speed to ensure the correct Reynolds number was achieved. The lift and drag voltages were recorded, with care taken to tare out the zero lift and drag voltages. This process was repeated for each of the remaining cant angles.

D. XFLR5 Simulation

The wing was replicated in XFLR5 using the integrated plane design tool. The cant angle of the airfoil section was adjusted in XFLR5 using the dihedral angle option in the wing design section. The analysis method employed was the ring vortex method, with an airspeed of 20 m/s. The simulation was performed at an angle of attack of 10 degrees, to replicate the experimental setup. The coefficients of lift and drag were recorded for each cant angle during the simulation.

III. RESULTS

The ambient pressure, P_{amb} , of the room was measured using a wall-mounted barometer. The temperature, T , and the relative humidity, φ , of the room was measured using a digital thermometer and hygrometer placed next to the test section. The measured atmospheric conditions are summarized in Table I.

TABLE I
ATMOSPHERIC CONDITIONS

Parameter	Value	Uncertainty (\pm)
P_{amb}	764.10 mmHg	0.02 mmHg
T	22.9 °C	0.1 °C
φ	40%	1%

To calibrate the dynamometer for lift and drag force measurements, twelve different mass configurations were used. These masses were loaded on the dynamometer in both its drag and lift configurations, as shown in Fig. 4 and 5, respectively. The masses were then converted into weights and plotted against their corresponding voltages for lift and drag as illustrated in Fig. 7 and 8, respectively.

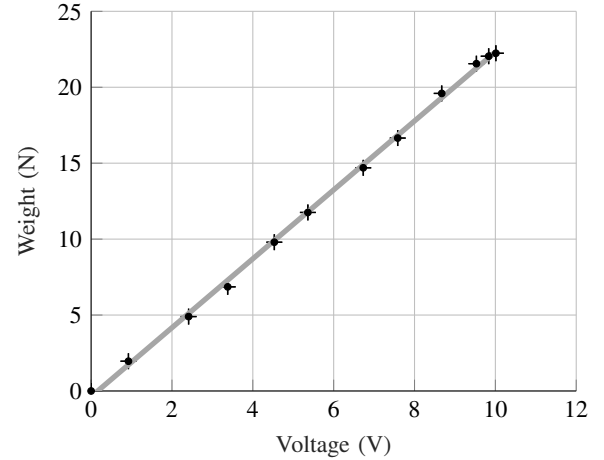


Fig. 7. Lift voltage calibration plot with twelve weights plotted against the resulting voltages.

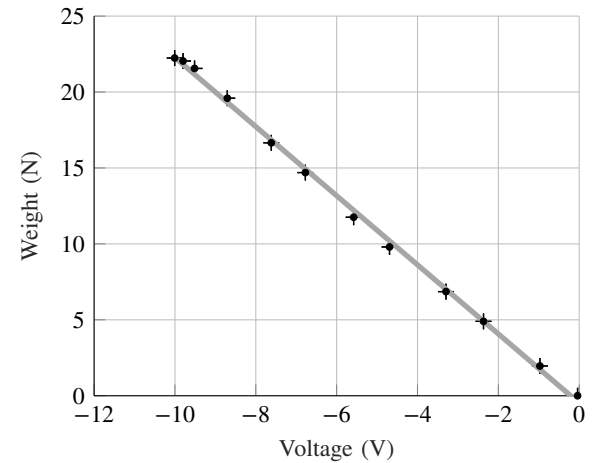


Fig. 8. Drag voltage calibration plot with twelve weights plotted against the resulting voltages.

The wind tunnel was operated at a Reynolds number of 102000 ± 287 , which was calculated using the dimensions of the airfoil section given in Table II. The chord length, c , the static pressure difference, ΔP , the zero-weight voltage for lift, $V_{L,\text{tare}}$, and the zero-weight voltage for drag, $V_{D,\text{tare}}$, were recorded before experimenting. These values are tabulated in Table II. The lift and drag voltages for each cant angle are shown in Table III.

TABLE II
REYNOLDS NUMBER CALCULATION VARIABLES

Parameter	Value	Uncertainty (\pm)
c	76.2 mm	0.5 mm
ΔP	1.642 inH ₂ O	0.002 inH ₂ O
$V_{L\text{tare}}$	-8.203 V	0.040 V
$V_{D\text{tare}}$	3.762 V	0.018 V

TABLE III
LIFT AND DRAG VOLTAGES

Cant Angle (deg)	Lift Voltage (V)	Drag Voltage (V)
0	-9.006 \pm 0.003	3.494 \pm 0.001
10	-9.010 \pm 0.003	3.494 \pm 0.001
20	-9.010 \pm 0.003	3.494 \pm 0.001
30	-9.011 \pm 0.003	3.495 \pm 0.001
40	-9.014 \pm 0.003	3.495 \pm 0.001
50	-9.010 \pm 0.003	3.495 \pm 0.001
60	-8.998 \pm 0.003	3.496 \pm 0.001
70	-8.998 \pm 0.003	3.495 \pm 0.001
80	-8.997 \pm 0.003	3.495 \pm 0.001
90	-8.997 \pm 0.003	3.493 \pm 0.001

Using the XFLR5 airfoil section model and the analysis settings, the lift-to-drag ratio was determined for each cant angle at an angle of attack of 10 degrees. These results were then plotted against each other in Fig. 9.

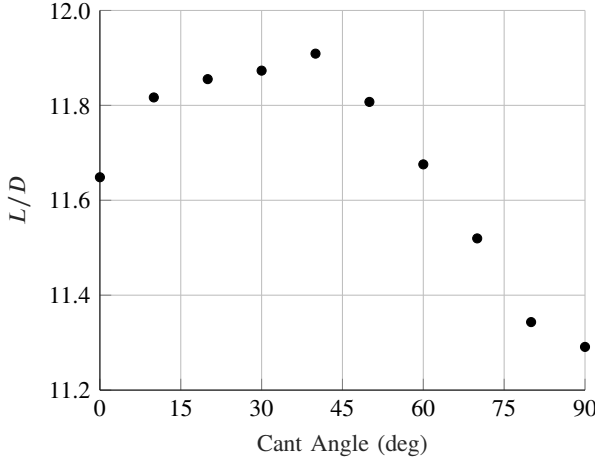


Fig. 9. The lift-to-drag ratio of the airfoil section at various cant angles as calculated by XFLR5.

IV. DISCUSSION

A. Comparison of Experimental Data to XFLR5 Data

Generally, the experimental data exhibited the expected shape, which included a peak occurring at a cant angle of approximately 40° and a subsequent decrease in the lift-to-drag ratio following this peak. The increase in the lift-to-drag ratio observed at cant angles below 40° aligned with the theory that

the presence of the winglets disrupted the wingtip vortices, resulting in an increase in the lift-to-drag ratio. Conversely, the decrease observed at high cant angles was consistent with the expectation that, at high cant angles, the increase in skin friction would outweigh the positive effects of implementing winglets in terms of the lift-to-drag ratio.

Another observation is that the experimental data consistently yielded lower lift-to-drag ratios compared to the theoretical XFLR5 data for each cant angle, as illustrated by Fig. 10. The percentage deviation between the experimental data and the XFLR5 data ranged from 6.4% to 14.1%. This discrepancy was attributed to the surface roughness in the wing caused by the FDM printing process, which created visible ridges in the wing. The surface roughness contributed to an increase in skin friction, consequently increasing the overall drag force experienced by the wing. Since the lift-to-drag ratio is inversely proportional to the drag force, this led to an underestimation of the overall lift-to-drag ratio as observed in the experimental data.

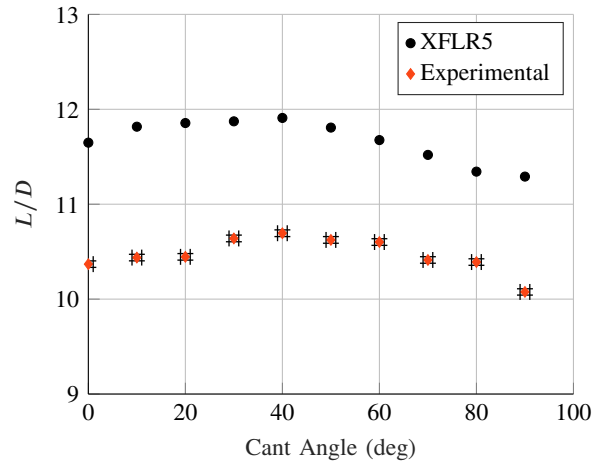


Fig. 10. Comparison of experimental lift-to-drag ratios with the theoretical ratios obtained from XFLR5 against varying cant angles.

B. Characterizing the Cant Angle Relationship

To determine an equation that would best represent the relationship between the winglet cant angle and the lift-to-drag efficiency ratio of the wing, several different theoretical models were tested to determine which was the most appropriate. The models considered included a linear, quadratic, cubic, and quartic model. The suitability of each model was assessed by analyzing the coefficient of determination obtained from performing a regression for each model. The coefficient of determination is a statistical variable used to evaluate how closely a linear regression matches the observed data [6]. For a given data set with dependent values y , the coefficient of determination, R^2 , can be determined using (2), where y_i denotes an individual data point, f_i is the predicted data point from the model, and \bar{y} is the mean of the data.

$$R^2 = 1 - \frac{\sum_i (y_i - f_i)^2}{\sum_i (y_i - \bar{y})^2} \quad (2)$$

Fig. 11, 12, 13, and 14 show the resulting regression models plotted on top of the experimental data.

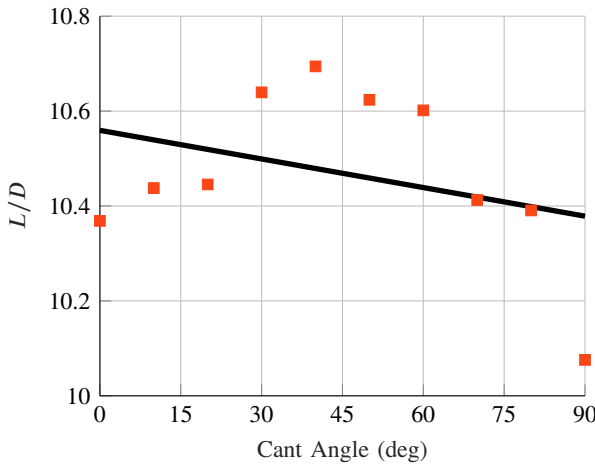


Fig. 11. Linear fit of the experimental data with $R^2 = 0.11$.

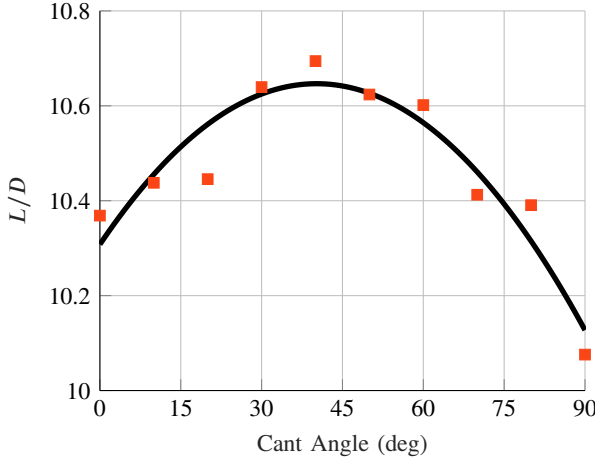


Fig. 12. Quadratic fit of the experimental data with $R^2 = 0.89$.

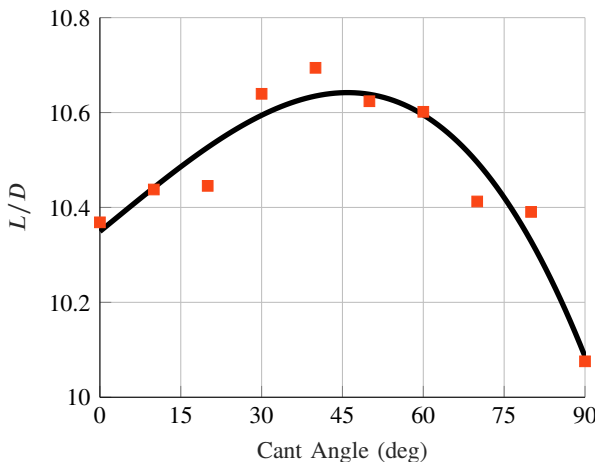


Fig. 13. Cubic fit of the experimental data with $R^2 = 0.92$.

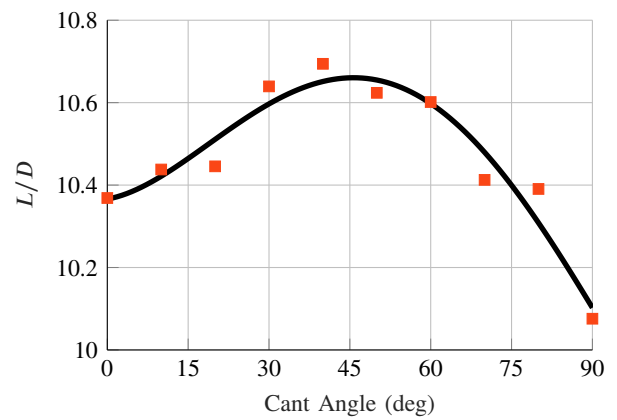


Fig. 14. Quartic fit of the experimental data with $R^2 = 0.93$.

The R^2 values for the four models are summarized in Table IV.

TABLE IV
COEFFICIENT OF DETERMINATION FOR EACH MODEL

Model	Coefficient of Determination, R^2
Linear	0.11
Quadratic	0.89
Cubic	0.92
Quartic	0.93

From Table IV, the quartic model was the most accurate in fitting the experimental data, followed by the cubic model. This finding is consistent with the visual analysis of Fig. 13 and 14, where both models appear to closely match the experimental data. The regression for the quartic model resulted in (3) for the best fit polynomial, where L/D_{quartic} is the predicted lift-to-drag ratio from the quartic model, and Γ is the cant angle.

$$\begin{aligned} L/D_{\text{quartic}} = & (4.0 \times 10^{-8})\Gamma^4 - (9.0 \times 10^{-6})\Gamma^3 \\ & + (4.0 \times 10^{-4})\Gamma^2 + (2.4 \times 10^{-3})\Gamma + 10.37 \end{aligned} \quad (3)$$

C. Determining the Optimal Winglet Cant Angle

To determine the theoretical optimal winglet cant angle, the local maximum of the quartic model was found. This was achieved by taking the derivative of the quartic model with respect to Γ , as shown in (4).

$$\begin{aligned} \frac{dL/D_{\text{quartic}}}{d\Gamma} = & (1.6 \times 10^{-7})\Gamma^3 - (2.7 \times 10^{-5})\Gamma^2 \\ & + (8.0 \times 10^{-4})\Gamma + 2.4 \times 10^{-3} \end{aligned} \quad (4)$$

A local extremum occurs when the first derivative is equal to zero. Setting (4) equal to zero and solving for the roots of Γ yields solutions at -2.74° , 42.36° , and 129.13° . Considering the bounds $0^\circ \leq \Gamma \leq 90^\circ$ from the experimental data, the local maximum occurs at $42 \pm 1^\circ$. The model exhibits a maximum percent error of 2.3% when compared to the experimental data. This error is associated with the 80° cant angle. The fact that the percent error generally increased for higher cant angles indicates that high cant angle winglets may make the flow more turbulent, causing variability in the aerodynamic forces.

V. CONCLUSION

Ultimately, it was found that the effect of winglet cant angle on the lift-to-drag ratio followed a quartic trend, with a peak occurring at an angle of about 40° . The increase in the lift-to-drag ratio before this peak is due to the winglets disrupting the formation of wingtip vortices, which reduces the induced drag. However, if the cant angle is increased beyond this peak, it results in additional skin friction and a decrease in the lift-to-drag ratio.

When comparing the experimental data to theoretical data obtained from XFLR5, it was observed that the shapes of both plots are similar, as shown in Fig. 10. However, the lift-to-drag ratios for the experimental data were consistently lower than those of the theoretical data. This is likely due to the presence of ridges on the surface of the wing from the 3D printing process. The increase in surface roughness caused by these ridges increased the total drag force acting on the wing. Using a different 3D printing method such as stereolithography would reduce the prominence of these ridges and would yield drag forces closer to the theoretical data.

Additionally, the method of mounting the wing to the dynamometer could be improved. In this experiment, tape was required to restrict the movement of the wing section, preventing it from spinning. To improve this, the orientation of the screw can be adjusted so that when fully threaded, the wing is in the correct orientation. This will eliminate any additional drag introduced by the tape.

To further expand on the results of the experiment, the tips of the airfoil can be modified so that they transition from an airfoil cross-section to a closed edge. This can be done by tapering the edge of the airfoil section until it forms a sharp edge. This modification will decrease the parasitic drag generated by the wingtip, thus increasing efficiency impact that the wingtip has on the wing and making any efficiency gains more pronounced.

APPENDIX A: UNCERTAINTY CALCULATIONS

TABLE V
SUMMARY OF MEASUREMENT UNCERTAINTIES

Parameter	Symbol	Justification	Uncertainty (\pm)
Temperature	μT	Digital	0.1 °C
Humidity	$\mu \varphi$	Digital	1%
Ambient Pressure	μP_{amb}	Barometer	0.02 mmHg
Static Pressure Difference	$\mu \Delta P$	95% Conf. Int.	0.55 Pa
Saturation Pressure	μP_g	RSS	15.22 Pa
Density	$\mu \rho$	RSS	0.004 kg/m ³
Airfoil Chord Length	μc	Calipers	0.2 mm
Tunnel Calibration Coefficient	μK	[5]	0.002
Kinematic Viscosity	$\mu \nu$	[7]	2×10^{-9} m ² /s
Reynolds Number	μRe	RSS	184.4
Lift	μL	Max. % Error	0.81%
Drag	μD	Max. % Error	0.94%
Lift-to-drag Ratio	$\mu L/D$	RSS	Variable
Cant Angle	$\mu \Gamma$	[8]	1°
Voltage	μV	[9]	0.05% of voltage

The uncertainties for each measured value are summarized in Table V. First, the systemic bias in the reading of the transducer static pressure readings was accounted for by zeroing the pressure value in the LabVIEW VI. The random uncertainty for each static pressure reading was then obtained by using a 95% confidence interval with a normal distribution. Because a sample size of 4000 was used for each reading, it was determined to be sufficiently large that the sample distribution approached the normal distribution according to the central limit theorem [10]. A z^* value of 1.96 was used for the calculation of the 95% confidence interval. The margin of error then served as the uncertainty, as seen in (5), where μX is the margin of error for an arbitrary measurement, S_x is the sample standard deviation, and n is the number of samples [10].

$$\mu X = z^* \frac{S_x}{\sqrt{n}} \quad (5)$$

The uncertainty in the saturation pressure, P_g , was calculated using error propagation theory, as shown by (6), where T is the ambient temperature [11].

$$\mu P_g = \mu T \frac{\partial P_g}{\partial T} \quad (6)$$

The uncertainty in the fluid density, ρ , was calculated using the RSS method, as shown by (7), where P is the ambient pressure, T is the ambient temperature, φ is the relative humidity, and P_g is the saturation pressure.

$$\mu \rho = \left[\left(\mu P \frac{\partial \rho}{\partial P} \right)^2 + \left(\mu T \frac{\partial \rho}{\partial T} \right)^2 + \left(\mu \varphi \frac{\partial \rho}{\partial \varphi} \right)^2 + \left(\mu P_g \frac{\partial \rho}{\partial P_g} \right)^2 \right]^{1/2} \quad (7)$$

The uncertainty in the Reynolds number, Re , was calculated using the RSS method, as shown by (8), where ΔP is the static pressure difference, ν is the dynamic viscosity of the fluid, ρ is the density of the fluid, and c is the chord length of the airfoil.

$$\mu Re = \left[\left(\mu \Delta P \frac{\partial Re}{\partial \Delta P} \right)^2 + \left(\mu \nu \frac{\partial Re}{\partial \nu} \right)^2 + \left(\mu \rho \frac{\partial Re}{\partial \rho} \right)^2 + \left(\mu c \frac{\partial Re}{\partial c} \right)^2 \right]^{1/2} \quad (8)$$

The uncertainties in the lift and drag values obtained from the dynamometer were determined by calculating the maximum percent error deviation from the calibration curve. As an example, Fig. 7 displays the calibration data, as well as the line of best fit that relates the voltage data to the weight.

The percentage error between the actual calibration data and the line of best fit was calculated for each voltage point. It was determined that the line of best fit had a maximum percent error of 0.81% at worst. Therefore, it was assumed that the interpolated lift values obtained from the voltage measurements from the dynamometer would have a percent error of 0.81%. This uncertainty was applied to all the lift values in the experiment. A similar process was also conducted for the drag values.

The uncertainty in the lift-to-drag ratio, L/D , was calculated using the RSS method, as shown by (9), where L is the interpolated lift force, and D is the interpolated drag force.

$$\mu L/D = \left[\left(\mu L \frac{\partial L/D}{\partial L} \right)^2 + \left(\mu D \frac{\partial L/D}{\partial D} \right)^2 \right]^{1/2} \quad (9)$$

This lab report was typeset using **LATEX**.

REFERENCES

- [1] Federal Aviation Administration, “Air Traffic By The Numbers,” URL: https://www.faa.gov/air_traffic/by_the_numbers, Apr 2023.
- [2] Hall, N., “Winglets,” *National Aeronautics and Space Administration*, URL: <https://www1.grc.nasa.gov/beginners-guide-to-aeronautics/winglets/>, 2023.
- [3] Mylsamy, D., Thirumalai, Y., and Premkumar, P. S., “Performance Investigation of an Aircraft Wing at Various Cant Angles of Winglets using CFD Simulation,” *Altair Technology Conference 2015*, Bangalore, India, 2015.
- [4] Swargam, L., Kidron, M., Nandigam, M. L., and Dwivedi, Y. D., “Effect of Variable Cant Angle on Sweepback Wing,” *Reviews on Modern Technologies for Aircraft and Aero-Engines*, Vol. 1, No. 9, Apr 2022, pp. 61–68.
- [5] Borg, A., Lam, B., Latzko, A., “Wind Tunnel Calibration for Prediction of Testing Conditions,” *University of Florida*, 2023.
- [6] Glantz, S. A., Slinker, B. K., and Neilands, T. B., “Selecting the ‘Best’ Regression Model,” *Primer of Applied Regression and Analysis of Variance*, McGraw-Hill, New York, 2016, pp. 335–380.
- [7] Bergman, T. L., and Lavine, A. S., “Appendix A: Thermophysical Properties of Matter,” *Fundamentals of Heat and Mass Transfer*, Wiley, Hoboken, NJ, 2017, p. 911.
- [8] Markforged, “How to Create High Quality STL Files for 3D Prints,” URL: <https://markforged.com/resources/blog/how-to-create-high-quality-stl-files-for-3d-prints>.
- [9] Schaevitz Sensors HR Series Data Sheet, Measurement Specialties, Inc., Hampton, VA, 2015.
- [10] Ridgeway, S., “MOM_lab Uncertainty basics w tension,” *University of Florida* [PowerPoint slides], URL: <https://ufl.instructure.com/courses/447927/files/65674680>, 2022.
- [11] Ku, H. H., “Notes on the Use of Propagation of Error Formulas”, *Journal of Research of the National Bureau of Standards*, Vol. 70C, No. 4, 27 May 1966, pp. 263–273.